THE JOURNAL OF PHYSICAL CHEMISTRY C

Article

pubs.acs.org/JPCC

Resistive Switching Characteristics of Self-Aligned $BiMnO_3$ Nanodots

Yoonho Ahn,[†] Jong Yeog Son,[*,†] and Joonkyung Jang[*,‡]

[†]Department of Applied Physics and Institute of Natural Sciences, Kyung Hee University, Yongin 17104, Republic of Korea

[‡]Department of Nanoenergy Engineering, Pusan National University, Busan 46241, Republic of Korea

ABSTRACT: Resistive switching behavior has been observed mainly in transition metal oxides, particularly in the form of thin-film cells. In the present study, self-aligned, ferroelectric $BiMnO_3$ (BMO) cubic nanodots on an Nb-doped $SrTiO_3$ substrate were fabricated by pulsed laser deposition (PLD). The BMO nanodots showed the bipolar resistive switching as well as the typical piezoresponse characteristics. Significantly, H_2 annealing of BMO nanodots resulted in a striking difference between the low-resistance state (LRS) and the high-resistance state (HRS) as well as a decrease in the SET and RESET voltages compared to the nonannealed BMO nanodots. We suggest that the conductive filament model is the most likely mechanism for the resistive switching in the BMO nanodots. Concentration of oxygen vacancies plays a major role in the growth of conductive paths during the H_2 annealing process, leading to reduction of effective thickness in the BMO nanodots.

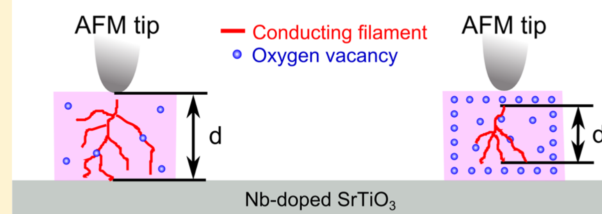

1. INTRODUCTION

Resistive random access memory (RRAM) is considered the next-generation memory owing to its low operation voltage, rapid switching speed, and simple structure.[1−6] The resistive switching characteristics, which are reproducible at two distinct states between a low-resistance state (LRS) and a high-resistance state (HRS), have been discovered in multiferroic materials such as $BiFeO_3$,[7,8] $Bi_{0.9}Ca_{0.1}FeO_3$,[9] and $BiCoO_3$[10] as well as transition metal oxides.[11−17] A range of RRAM materials exhibit two representative resistive switching, "unipolar" and "bipolar", modes, depending on the configurations of the RRAM capacitors.[1,2,18] Among the mechanisms proposed for the resistive switching behavior,[1,19−21] the most reliable is the conductive filament model. The filament-type resistive switching originates from the formation and rupture of filamentary conducting paths in insulating materials,[3,22−25] which have demonstrated both unipolar and bipolar switching behavior.

A few studies reported RRAM devices made from nanostructures, such as nanodots and nanowires.[12,26−28] The functionality of RRAM devices might be enhanced by scaling their sizes down to the nanometer scale. A nanoscale RRAM structure can be constructed using nanofabrication techniques, such as nanotemplate, dip-pen lithography, etc.[26,29] For example, an anodic aluminum oxide (AAO) nanotemplate was used to fabricate the Au/NiO/Au RRAM nanowire arrays, which exhibited unipolar RRAM switching behaviors with lower ON and OFF currents than in those previously reported utilizing the NiO RRAM microcapacitors.[26] The dip-pen lithography technique was also used to form NiO nanodots at the desired positions[29] In this work, the $BiMnO_3$ (BMO) nanodots were fabricated using the pulsed laser deposition (PLD) by controlling the deposition time. The resistive switching characteristics of self-aligned ferroelectric BMO nanodots on Nb-doped $SrTiO_3$ substrate were investigated. The BMO are known as multiferroics because it presents ferroelectric and ferromagnetic properties simultaneously.[30−33] In particular, the fact that the BMO is leaky electrically due to oxygen vacancies can make it easier and more applicable to RRAM devices.[34,35] BMO nanodots, 10 and 20 nm in diameter, exhibited typical piezoresponse (d_{33}) hysteresis loops and bipolar switching characteristics. The effects of hydrogen (H_2) annealing on the variation of SET and RESET voltages in the BFO nanodots were investigated further.

2. EXPERIMENTAL SECTION

Cubic BMO nanodots were deposited on the step and terrace surfaces of Nb-doped $SrTiO_3$ substrates by PLD, as shown schematically in Figure 1a. Aligned BMO nanodots were fabricated using the electrochemical step-edge decoration (ESED) technique,[36,37] which is commonly used to fabricate nanodots or nanowires on the terrace edges of single crystalline substrates. The BMO nanodots can be formed along the step edges of the terrace due to the fact that step edges are energetically more stable for nucleation of adatoms.[36] For the ESED of BMO nanodots, a Nb-doped STO substrate of an atomically flat and well-aligned terrace surface was used, which was prepared by HF treatments and an annealing process. The Nb-doped STO substrates were dipped in a dilute HF solution and annealed at 1000 °C for 1 h.[38]

A 1 in. BMO target was prepared using the conventional solid-state reaction method. High purity, commercially available powders of Bi_2O_3 (99.99%) and Mn_2O_3 (99.99%) were mixed

Received: April 15, 2016
Revised: May 12, 2016
Published: May 13, 2016

Downloaded via PUSAN NATL UNIV on May 16, 2020 at 12:51:22 (UTC).
See https://pubs.acs.org/sharingguidelines for options on how to legitimately share published articles.

ACS Publications © 2016 American Chemical Society

DOI: 10.1021/acs.jpcc.6b03827
J. Phys. Chem. C 2016, 120, 11739−11743

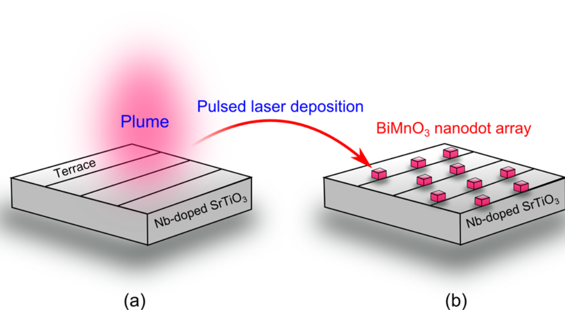

Figure 1. Schematic diagram of the $BiMnO_3$ nandots array on the Nb-doped $SrTiO_3$ substrate. (a) Pulsed laser deposition process of $BiMnO_3$. (b) $BiMnO_3$ nandots array at the terrace edges of the Nb-doped $SrTiO_3$ substrate.

after weighing out according to their stoichiometry. Owing to the volatility of bismuth during the film deposition process, the bismuth concentration was increased and the Bi to Mn molar ratio (1.1:1) was adjusted. The mixture was well ground, pelletized and calcined at 750 °C for 24 h. This process was repeated three times to form a dense ceramic target. A KrF excimer laser (wavelength of 248 nm and energy density of 0.5 J/cm^2) for PLD was focused onto a BMO target. The distance between the BMO target and substrate was approximately 40 mm. When the base pressure reached approximately 10^{-7} Torr, the substrate temperature and oxygen partial pressure were set to 800 °C and 0.2 Torr, respectively. After deposition, the samples were cooled to room temperature under 300 Torr oxygen ambient. The nominal deposition rate of the BMO was approximately 0.005 nm/pulse in PLD. Atomic force microscopy (AFM) was used to check the surface topography of each BMO nanodot array. Ferroelectric and resistive switching properties for the BMO nanodots were characterized by PFM and conductive atomic force microscopy (C-AFM) measurements, respectively.

3. RESULTS AND DISCUSSION

The cubic BMO nanodot arrays were fabricated by controlling their sizes using different PLD times. The cubic shape was observed as the size of the BMO nanodot increased, indicating a high degree of crystallinity. Figures 1a,b show schematic diagrams of the fabrication of $BiMnO_3$ nanodot arrays on a Nb-doped $SrTiO_3$ substrate. Arrays of 10 and 20 nm sized BMO nanodots were formed at PLD times of 45 and 180 s, respectively. Prior to BMO deposition, the Nb-doped $SrTiO_3$ substrate were confirmed to have a terrace surface with uniform intervals of approximately 70 nm and a low roughness below 0.2 nm by AFM.

First, the topography of two-sized BMO nanodot arrays was observed, as shown in Figures 2a,b. The AFM images showed that most of the BMO nanodots nucleated on the terrace edges of the Nb-doped $SrTiO_3$ substrate. For a PLD time of 45 s, the 10 nm sized BMO nanodots were mainly formed. A range of BMO nanodots, large and small in size, were also observed at the terrace surface (Figure 2a). In the case of very tiny BMO nanodots (approximately a few nanometer sizes), however, a high leakage current was measured in the PFM measurement. Therefore, only the 10 nm sized BMO nanodots were considered for the PFM measurement. To make larger BMO nanodots, the deposition time of the PLD was increased. Doubling the size of the 10 nm sized BMO nanodots took 180 s. Similar to the 10 nm sized BMO nanodots, the 20 nm sized

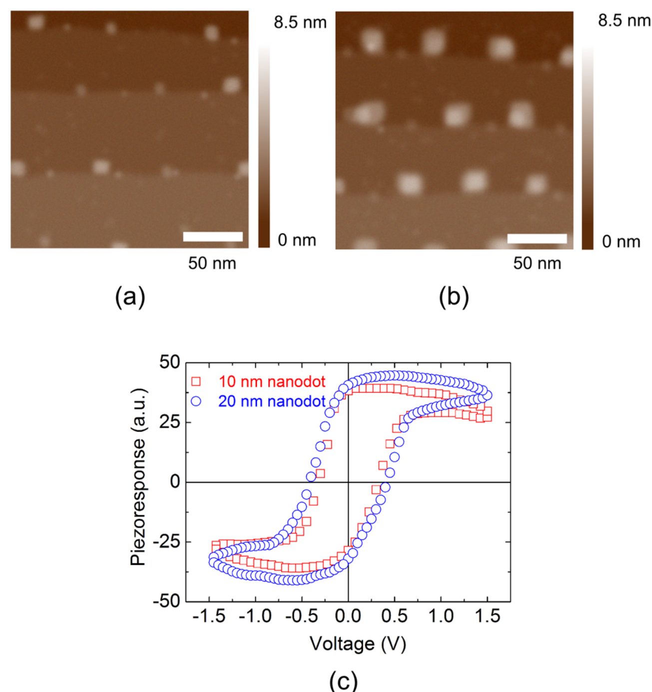

Figure 2. AFM images of two-sized $BiMnO_3$ nanodots arrays of (a) 10 nm and (b) 20 nm. (c) Piezoresponse (d_{33}) hysteresis loops of two-sized $BiMnO_3$ nanodots of 10 and 20 nm.

BMO nanodots were well aligned along the edges of the terraces, as shown in Figure 2b.

Figure 2c shows d_{33} curves for the 10 and 20 nm sized BMO nanodots as a function of the applied voltage. Both BMO nanodots exhibited the typical piezoresponse hysteresis loops as a ferroelectric material, in which the d_{33} value of the 20 nm sized BMO nanodot was larger than that of the 10 nm sized BMO nanodot at a zero voltage. This is because the 10 nm sized BMO nanodot has a larger leakage current than the 20 nm sized BMO nanodot. On the other hand, the 10 nm sized BMO nanodot showed a lower coercive voltage than the 20 nm sized BMO nanodot. This low coercive voltage of the 10 nm sized BMO nanodot is due to the size effects of ferroelectric nanodots as well as the low d_{33} value with scaling down.[1,39,40]

Figure 3a presents the current−voltage (I−V) characteristic curves of the BMO nanodots, which exhibit typical resistive switching behaviors with two different resistance states between the HRS and LRS. The measurement was conducted at room temperature under atmospheric condition. By applying a voltage ramp, forming voltages of 10 and 20 nm sized BMO

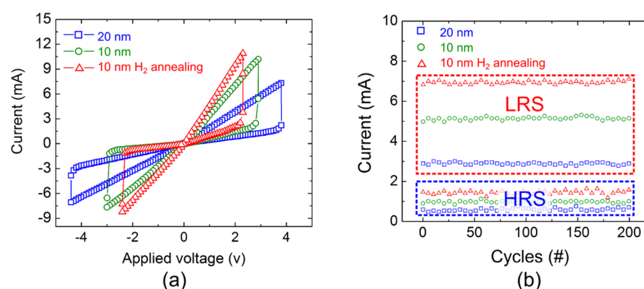

Figure 3. (a) Typical resistive switching characteristics of $BiMnO_3$ nanodots. (b) Bistable resistivity as a function of the switching cycles of the $BiMnO_3$ nanodots.

DOI: 10.1021/acs.jpcc.6b03827
J. Phys. Chem. C 2016, 120, 11739−11743

nanodots were measured to be 3.8 and 3 V, respectively. During the dc voltage sweep, the BMO nanodots exhibited bipolar switching characteristics with symmetric hysteresis; it changed from the HRS to the LRS under a positive bias and from the LRS to the HRS under a negative bias. In the case of the 10 nm sized BMO nanodot, the current increased suddenly at +2.9 V, where the resistive state switches from the HRS to the LRS (SET process). On the other hand, the current decreased dramatically at −3 V, which refers to the resistive change from the LRS to the HRS (RESET process). The 20 nm sized BMO nanodot exhibited SET and RESET voltages of +3.8 and −4.3 V, respectively, which means that the SET and RESET voltages increase with increasing nanodot size. Generally, the SET and RESET voltages can decrease with increasing concentration of oxygen vacancies in transition metal oxides.[1,18] In addition, the leakage current increases with decreasing the size of nanodots. Therefore, the 10 nm sized BMO have a higher leakage current than that of the 20 nm sized BMO nanodot. Because the slopes in the $I-V$ curve are proportional to the resistances of the HRS and LRS, the 10 nm sized BMO shows a clearer difference between the HRS and LRS compared to the 20 nm sized BMO nanodot.

The influence of oxygen vacancies on the SET and RESET voltages in the 10 nm sized BMO nanodot was investigated further. The 10 nm sized BMO nanodots were annealed to increase the population of oxygen vacancies. For this, a forming gas (H_2, 20 mTorr) annealing process was conducted at 500 °C for 10 min. After the H_2 annealing process, the $I-V$ characteristics were measured (Figure 3a). The SET and RESET voltages of the H_2-annealed (10 nm sized) BMO nanodot were −2.3 and +2.2 V, respectively. As expected, these voltages are smaller than those of the nonannealed BMO nanodot. Therefore, the H_2-annealed BMO nanodot has a higher leakage current than the nonannealed BMO nanodot. In Figure 3a, the H_2-annealed (10 nm sized) BMO nanodot showed the lowest LRS state and the largest difference between the LRS and HRS. Significantly, H_2 annealing of the BMO nanodot maximized the difference between the LRS and HRS, leading to a decrease in SET and RESET voltages.

To check the reproducible switching behavior of the BMO nanodots, the bistable resistivities were obtained as a function of the switching cycle, where the reading voltage was 1.5 V (Figure 3b). For the two sized and H_2-annealed BMO nanodots, the different current states were stable and reproducible when the number of switching cycles was increased to 200 cycles. In particular, the H_2-annealed BMO nanodot also exhibited the largest difference between the ON and OFF currents.

As mentioned previously, the resistive switching behavior in the BMO nanodots is related to filamentary conducting paths. The oxygen vacancies, which occur mainly in perovskite oxides concomitantly with Bi vacancies due to its volatile property, would induce conductive paths (filaments), leading to a metallic state.[41,42] Figure 4 presents schematic drawings for the formation of oxygen vacancies after the H_2 annealing process as well as the features of the conducting filaments depending on the population of oxygen vacancies. Please note that the H_2 concentration plays the role as a catalyst in ferroelectric oxides, leading to oxygen vacancies and other positive charge centers.[43] In other words, lattice defects in the BMO nanodot are generated by H_2 annealing, which are likely to be oxygen and Bi vacancies. In particular, oxygen vacancies are concentrated at the surface of the BMO nanodot (Figure 4a). The region distributed with a high concentration of oxygen vacancies is electrically more conductive because oxygen vacancies give rise to an effect that is equivalent to "electron doping". Therefore, the H_2 annealing process results in two features. First, the oxygen vacancies increase the likelihood of the formation of conduction filaments during the SET and RESET switching process. Second, oxygen vacancies reduce the effective thickness (d) of the BMO nanodot (Figure 4b). This means that the effective electric field is enhanced by the gradual growth of conductive filaments in the oxygen vacancy-concentrated region compared to the non-H_2-annealed BMO nanodot.

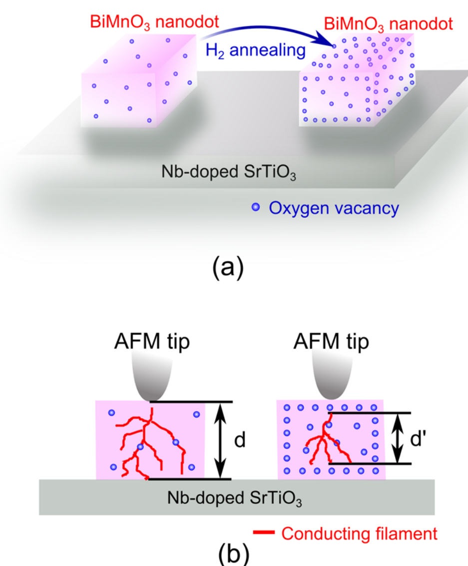

Figure 4. Schematic diagram of (a) the formation of oxygen vacancies after the H_2 annealing process and (b) features of the conducing filaments depending on the concentrations of oxygen vacancies. The effective thickness (d) of BMO nanodot is reduced after the H_2 annealing process.

4. CONCLUSIONS

This study examined the RRAM characteristics of the self-aligned ferroelectric BMO nanodots. They were fabricated at the terrace edges of the Nb-doped $SrTiO_3$ substrate by pulsed laser deposition. PFM and C-AFM were used to identify the ferroelectric and resistive switching characteristics, in which the 10 and 20 nm sized ferroelectric BMO nanodots exhibited typical ferroelectric d_{33} hysteresis loops and bipolar switching behaviors. The H_2 annealing process made it possible to maximize the difference between the LRS and HRS and reduce the SET and RESET voltages. This study provides insight into nanodot RRAM devices.

■ AUTHOR INFORMATION

Corresponding Authors

*E-mail jyson@khu.ac.kr; Tel +82-31-201-3770 (J.Y.S.).

*E-mail jkjang@pusan.ac.kr; Tel +82-51-510-7348 (J.J.).

Notes

The authors declare no competing financial interest.

■ ACKNOWLEDGMENTS

This study was supported by the National Research Foundation of Korea (NRF) grant funded by the Korea government

(MSIP) (Nos. 2015R1A2A2A05027951 and 2015R1A2A2A01004208).

■ REFERENCES

(1) Sawa, A. Resistive Switching in Transition Metal Oxides. *Mater. Today* **2008**, *11*, 28−36.
(2) Akinaga, H.; Shima, H. Resistive Random Access Memory (ReRAM) Based on Metal Oxides. *Proc. IEEE* **2010**, *98*, 2237−2251.
(3) Kinoshita, K.; Tamura, T.; Aoki, M.; Sugiyama, Y.; Tanaka, H. Bias Polarity Dependent Data Retention of Resistive Random Access Memory Consisting of Binary Transition Metal Oxide. *Appl. Phys. Lett.* **2006**, *89*, 103509.
(4) Lee, M.-J.; Han, S.; Jeon, S. H.; Park, B. H.; Kang, B. S.; Ahn, S.-E.; Kim, K. H.; Lee, C. B.; Kim, C. J.; Yoo, I.-K.; Seo, D. H.; Li, X.-S.; Park, J.-B.; Lee, J.-H.; Park, Y. Electrical Manipulation of Nanofilaments in Transition-Metal Oxides for Resistance-Based Memory. *Nano Lett.* **2009**, *9*, 1476−1481.
(5) Lee, M.-J.; Lee, C. B.; Lee, D.; Lee, S. R.; Chang, M.; Hur, J. H.; Kim, Y.-B.; Kim, C.-J.; Seo, D. H.; Seo, S.; Chung, U. I.; Yoo, I.-K.; Kim, K. A Fast, High-Endurance and Scalable Non-Volatile Memory Device Made from Asymmetric Ta_2O_{5-x}/TaO_{2-x} Bilayer Structures. *Nat. Mater.* **2011**, *10*, 625−630.
(6) Pan, F.; Gao, S.; Chen, C.; Song, C.; Zeng, F. Recent Progress in Resistive Random Access Memories: Materials, Switching Mechanisms, and Performance. *Mater. Sci. Eng., R* **2014**, *83*, 1−59.
(7) Wang, C.; Jin, K.-j.; Xu, Z.-t.; Wang, L.; Ge, C.; Lu, H.-b.; Guo, H.-z.; He, M.; Yang, G.-z. Switchable Diode Effect and Ferroelectric Resistive Switching in Epitaxial $BiFeO_3$ Thin Films. *Appl. Phys. Lett.* **2011**, *98*, 192901.
(8) Kim, W.-H.; Son, J. Y.; Jang, H. M. Confinement of Ferroelectric Domain-Wall Motion at Artificially Formed Conducting-Nanofilaments in Epitaxial $BiFeO_3$ Thin Films. *ACS Appl. Mater. Interfaces* **2014**, *6*, 6346−6350.
(9) Rubi, D.; Gomez-Marlasca, F.; Bonville, P.; Colson, D.; Levy, P. Resistive Switching in Ceramic Multiferroic $Bi_{0.9}Ca_{0.1}FeO_3$. *Phys. B* **2012**, *407*, 3144−3146.
(10) Sun, B.; Li, Q.; Liu, Y.; Chen, P. Resistive Switching of Multiferroic $BiCoO_3$ Nanoflowers. *Funct. Mater. Lett.* **2015**, *08*, 1550001.
(11) Son, J. Y.; Shin, Y. H. Direct Observation of Conducting Filaments on Resistive Switching of NiO Thin Films. *Appl. Phys. Lett.* **2008**, *92*, 222106.
(12) Son, J. Y.; Shin, Y. H.; Kim, H.; Jang, H. M. NiO Resistive Random Access Memory Nanocapacitor Array on Graphene. *ACS Nano* **2010**, *4*, 2655−2658.
(13) Bharti, S.; Mehta, B. R.; Deepak, V.; Andreea Veronica, S.; Juergen, B. CAFM Investigations of Filamentary Conduction in Cu_2O ReRAM Devices Fabricated Using Stencil Lithography Technique. *Nanotechnology* **2012**, *23*, 495707.
(14) Choi, B. J.; Jeong, D. S.; Kim, S. K.; Rohde, C.; Choi, S.; Oh, J. H.; Kim, H. J.; Hwang, C. S.; Szot, K.; Waser, R.; Reichenberg, B.; Tiedke, S. Resistive Switching Mechanism of TiO_2 Thin Films Grown by Atomic-Layer Deposition. *J. Appl. Phys.* **2005**, *98*, 033715.
(15) Sawa, A.; Fujii, T.; Kawasaki, M.; Tokura, Y. Hysteretic Current−Voltage Characteristics and Resistance Switching at a Rectifying $Ti/Pr_{0.7}Ca_{0.3}MnO_3$ Interface. *Appl. Phys. Lett.* **2004**, *85*, 4073−4075.
(16) Watanabe, Y.; Bednorz, J. G.; Bietsch, A.; Gerber, C.; Widmer, D.; Beck, A.; Wind, S. J. Current-Driven Insulator−Conductor Transition and Nonvolatile Memory in Chromium-Doped $SrTiO_3$ Single Crystals. *Appl. Phys. Lett.* **2001**, *78*, 3738−3740.
(17) Beck, A.; Bednorz, J. G.; Gerber, C.; Rossel, C.; Widmer, D. Reproducible Switching Effect in Thin Oxide Films for Memory Applications. *Appl. Phys. Lett.* **2000**, *77*, 139−141.
(18) Ilia, V.; Rainer, W.; John, R. J.; Michael, N. K. Electrochemical Metallization Memories Fundamentals, Applications, Prospects. *Nanotechnology* **2011**, *22*, 254003.
(19) Pan, F.; Chen, C.; Wang, Z.-s.; Yang, Y.-c.; Yang, J.; Zeng, F. Nonvolatile Resistive Switching Memories-Characteristics, Mechanisms and Challenges. *Prog. Nat. Sci.* **2010**, *20*, 1−15.
(20) Doo Seok, J.; Reji, T.; Katiyar, R. S.; Scott, J. F.; Kohlstedt, H.; Petraru, A.; Cheol Seong, H. Emerging Memories: Resistive Switching Mechanisms and Current Status. *Rep. Prog. Phys.* **2012**, *75*, 076502.
(21) Waser, R.; Aono, M. Nanoionics-Based Resistive Switching Memories. *Nat. Mater.* **2007**, *6*, 833−840.
(22) Russo, U.; Ielmini, D.; Cagli, C.; Lacaita, A. L. Filament Conduction and Reset Mechanism in NiO-Based Resistive-Switching Memory (RRAM) Devices. *IEEE Trans. Electron Devices* **2009**, *56*, 186−192.
(23) Chen, J.-Y.; Hsin, C.-L.; Huang, C.-W.; Chiu, C.-H.; Huang, Y.-T.; Lin, S.-J.; Wu, W.-W.; Chen, L.-J. Dynamic Evolution of Conducting Nanofilament in Resistive Switching Memories. *Nano Lett.* **2013**, *13*, 3671−3677.
(24) Yang, Y.; Gao, P.; Gaba, S.; Chang, T.; Pan, X.; Lu, W. Observation of Conducting Filament Growth in Nanoscale Resistive Memories. *Nat. Commun.* **2012**, *3*, 732.
(25) Yao, J.; Zhong, L.; Natelson, D.; Tour, J. M. In Situ Imaging of the Conducting Filament in a Silicon Oxide Resistive Switch. *Sci. Rep.* **2012**, *2*, 242.
(26) Perego, D.; Franz, S.; Bestetti, M.; Cattaneo, L.; Brivio, S.; Tallarida, G.; Spiga, S. Engineered Fabrication of Ordered Arrays of Au-NiO-Au Nanowires. *Nanotechnology* **2013**, *24*, 045302.
(27) Oka, K.; Yanagida, T.; Nagashima, K.; Kawai, T.; Kim, J.-S.; Park, B. H. Resistive-Switching Memory Effects of NiO Nanowire/Metal Junctions. *J. Am. Chem. Soc.* **2010**, *132*, 6634−6635.
(28) Oka, K.; Yanagida, T.; Nagashima, K.; Tanaka, H.; Kawai, T. Nonvolatile Bipolar Resistive Memory Switching in Single Crystalline NiO Heterostructured Nanowires. *J. Am. Chem. Soc.* **2009**, *131*, 3434−3435.
(29) Kim, W.-H.; Park, C. S.; Son, J. Y. Nanoscale Resistive Switching Memory Device Composed of NiO Nanodot and Graphene Nanoribbon Nanogap Electrodes. *Carbon* **2014**, *79*, 388−392.
(30) Chi, Z. H.; Xiao, C. J.; Feng, S. M.; Li, F. Y.; Jin, C. Q.; Wang, X. H.; Chen, R. Z.; Li, L. T. Manifestation of Ferroelectromagnetism in Multiferroic $BiMnO_3$. *J. Appl. Phys.* **2005**, *98*, 103519.
(31) Montanari, E.; Righi, L.; Calestani, G.; Migliori, A.; Gilioli, E.; Bolzoni, F. Room Temperature Polymorphism in Metastable $BiMnO_3$ Prepared by High-Pressure Synthesis. *Chem. Mater.* **2005**, *17*, 1765−1773.
(32) Jeen, H.; Singh-Bhalla, G.; Mickel, P. R.; Voigt, K.; Morien, C.; Tongay, S.; Hebard, A. F.; Biswas, A. Growth and Characterization of Multiferroic $BiMnO_3$ Thin Films. *J. Appl. Phys.* **2011**, *109*, 074104.
(33) Lee, B.; Yoo, P.; Nam, V.; Toreh, K.; Jung, C. Magnetic and Electric Properties of Stoichiometric $BiMnO_3$ Thin Films. *Nanoscale Res. Lett.* **2015**, *10*, 47.
(34) Son, J. Y.; Kim, B. G.; Kim, C. H.; Cho, J. H. Writing Polarization Bits on the Multiferroic $BiMnO_3$ Thin Film using Kelvin Probe Force Microscope. *Appl. Phys. Lett.* **2004**, *84*, 4971−4973.
(35) Eerenstein, W.; Morrison, F. D.; Sher, F.; Prieto, J. L.; Attfield, J. P.; Scott, J. F.; Mathur, N. D. Experimental Difficulties and Artefacts in Multiferroic and Magnetoelectric Thin Tilms of $BiFeO_3$, $Bi_{0.6}Tb_{0.3}La_{0.1}FeO_3$ and $BiMnO_3$. *Philos. Mag. Lett.* **2007**, *87*, 249−257.
(36) Zach, M. P.; Ng, K. H.; Penner, R. M. Molybdenum Nanowires by Electrodeposition. *Science* **2000**, *290*, 2120−2123.
(37) Walter, E. C.; Murray, B. J.; Favier, F.; Kaltenpoth, G.; Grunze, M.; Penner, R. M. Noble and Coinage Metal Nanowires by Electrochemical Step Edge Decoration. *J. Phys. Chem. B* **2002**, *106*, 11407−11411.
(38) Kawasaki, M.; Takahashi, K.; Maeda, T.; Tsuchiya, R.; Shinohara, M.; Ishiyama, O.; Yonezawa, T.; Yoshimoto, M.; Koinuma, H. Atomic Control of the $SrTiO_3$ Crystal Surface. *Science* **1994**, *266*, 1540−1542.
(39) Buhlmann, S.; Dwir, B.; Baborowski, J.; Muralt, P. Size Effect in Mesoscopic Epitaxial Ferroelectric Structures: Increase of Piezoelectric Response with Decreasing Feature Size. *Appl. Phys. Lett.* **2002**, *80*, 3195−3197.

DOI: 10.1021/acs.jpcc.6b03827
J. Phys. Chem. C 2016, 120, 11739−11743

(40) Son, J. Y.; Shin, Y.-H.; Ryu, S.; Kim, H.; Jang, H. M. Dip-Pen Lithography of Ferroelectric $PbTiO_3$ Nanodots. *J. Am. Chem. Soc.* **2009**, *131*, 14676−14678.
(41) Szot, K.; Speier, W.; Bihlmayer, G.; Waser, R. Switching the Electrical Resistance of Individual Dislocations in Single-Crystalline $SrTiO_3$. *Nat. Mater.* **2006**, *5*, 312−320.
(42) Sarhan, A.; Nakanishi, H.; Diño, W. A.; Kishi, H.; Kasai, H. Oxygen Vacancy Effects on Electronic Structure of Pt/NiO/Pt Capacitor-Like System. *Surf. Sci.* **2012**, *606*, 239−246.
(43) Scott, J. F.; Redfern, S. A. T.; Zhang, M.; Dawber, M. Polarons, Oxygen Vacancies, and Hydrogen in $Ba_xSr_{1-x}TiO_3$. *J. Eur. Ceram. Soc.* **2001**, *21*, 1629−1632.

DOI: 10.1021/acs.jpcc.6b03827
J. Phys. Chem. C 2016, 120, 11739−11743